

# Continuous Control Set Model Predictive Control of a Modular Multilevel Converter for Drive Applications

Yeiner Arias-Esquivel, *Student Member, IEEE*, Roberto Cárdenas, *Senior Member, IEEE*, Matías Urrutia, *Student Member, IEEE*, Matias Diaz, *Member, IEEE*, Luca Tarisciotti, *Senior Member, IEEE*, and Jon C. Clare, *Senior Member, IEEE*

**Abstract**—The Modular Multilevel Converter is a good alternative for high power, medium voltage drive applications due to its modularity and scalability. However, the control is complex and typically involves several highly-coupled circulating current feedback loops implemented using Single-Input Single-Output design tools. Additionally, each circulating current has many different frequency components and electrical sequences to increase the degrees of freedom in the controller. In this work, the use of Continuous Control Set Model Predictive Control is proposed in order to include cross-coupling and interactions between the state variables and consider the system constraints, such as maximum current and maximum output voltage. The controller is intended for drive applications and is designed to operate with good dynamic performance over the entire speed range of the machine. The control methodology proposed is experimentally validated using an 18-cell MMC prototype driving a cage machine. Additional experimental tests are performed using PLECS-RT HIL platforms.

**Index Terms**—Modular Multilevel Converter, Model Predictive Control, Variable Speed Drives, Voltage Balancing, Weighting Factor, Online Tuning.

## I. INTRODUCTION

THE Modular Multilevel Converter (MMC) was proposed by Marquardt in 2003 [1], for high-voltage DC transmission [2], [3]. However, in recent years its use has been extended to applications such as Medium-Voltage Motor Drives, Power Quality Improvement [4], [5], etc. The popularity of this converter for high-power applications is due, among other reasons, to its power and voltage scalability, high efficiency and reduced  $dv/dt$  in the voltages [3]. The MMC topology is shown in Fig. 1; the converter is composed of six clusters, an AC port, a DC port, and six inductors. Each cluster consists of “ $n$ ” half-bridges each of them equipped with a floating capacitor.

Control of the MMC is complex, considering the Multiple-Input Multiple-Output (MIMO) characteristic of the converter, where multiple control objectives have to be achieved. For example, it is necessary to regulate the voltage of the floating capacitors, balance the energy stored in each arm, regulate the circulating currents, and control the currents and voltages at the AC and DC ports [3], [6]. As reported in several publications (e.g. [4], [7], [8]) this is difficult to achieve for drive applications, particularly when the output frequency at the AC port is low [3], [9], [10]. For these applications, the operating range is typically divided into two modes, namely Low-Frequency Mode (LFM) and High-Frequency

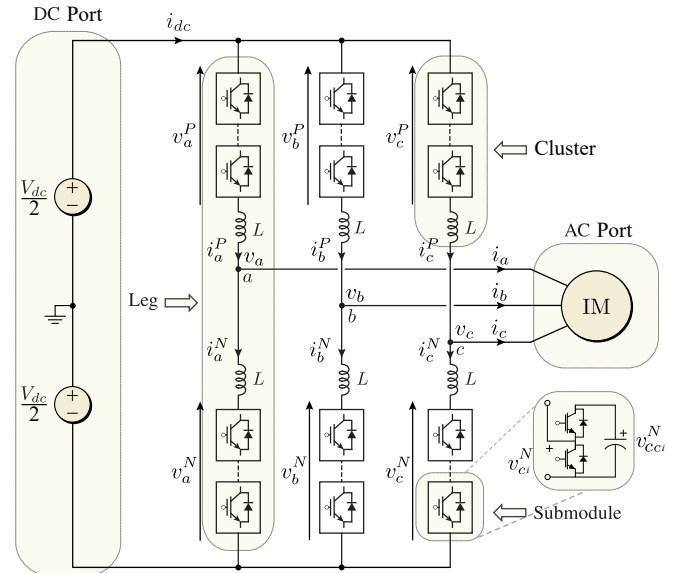


Fig. 1. Modular Multilevel Converter Topology.

Mode (HFM) [4], [6], [9]. Each of these operating modes requires a different control strategy typically based on multiple Single-Input Single-Output (SISO) designed control loops. Although LFM and HFM separation provides control of an MMC-based drive over the entire operating range [4], [7], [10], better dynamic performance can be achieved using MIMO controllers [11].

The MMC has six energy components which have to be actively balanced, to control the total energy stored in the MMC capacitors [12] and to achieve LFM or HFM operation. For example, during HFM, two circulating currents are utilised for energy balancing purposes; however each circulating current comprises a DC component, a positive sequence AC component and a negative sequence AC component [4]. The solution normally proposed in the literature is to design the controllers neglecting cross-coupling between the energies and the circulating current components (e.g. see [7], [13]), rendering sub-optimal performance [14], [15]. To improve the control performance, MIMO controllers have been proposed in [14]. Nevertheless, conventional MIMO controllers cannot include constraints such as maximum current and maximum output voltage in each arm [15]; moreover, saturation limitation of the currents and voltages is difficult to achieve even in the case of decoupled SISO controllers. For instance, as demonstrated in [12], the implementation of anti wind-up schemes to limit

separate components of the circulating currents, renders a sub-optimal saturation performance for the total current.

Recently, Model Predictive Control (MPC) has been proposed for power converter control due to its flexibility and simplicity [16], [17]. MPC algorithms can be designed to include multiple constraints, achieving a fast dynamic response, and can be applied to MIMO systems [5], [18]. For power electronic applications, the most widely used MPC methodology is based on Finite Control Set (FCS) algorithms or FCS-MPC [19]. However, FCS-MPC schemes produce variable switching frequency [20], [21] and, for converter structures with a high number of switching states, may result in an unfeasible computational burden for the control platform (see [5]). Conversely, a Continuous Control Set (CCS) MPC algorithm offers a constant switching frequency [22] and the external modulation stage reduces the computational burden [15], [23] of the MPC algorithm. In fact, unlike the conventional FCS-MPC applications to MMC, where the computer burden is heavily dependent on the total number of SMs (see [5], [22]), the computer burden of the proposed CCS-MPC is relatively low and has an almost fixed value which is independent of the number of half-bridge cells.

There are relatively few publications proposing CCS-MPC algorithms for MMC control. In [22], a simplified optimisation problem with only two constraints is proposed and graphically solved. In [15], more constraints are used to limit the total currents in the MMC and the arm voltages. A MATLAB solver is used in [15] to obtain the solution of the optimisation problem and the proposed methodology has been validated using simulation. Neither [22], nor [15] discuss control methods that can be applied to MMC-based drives where the voltage and frequency at the AC port are variable.

In this work a two-stage CCS-MPC algorithm is proposed. The outer CCS-MPC regulates the MMC capacitor voltages while the inner CCS-MPC regulates the currents. The decoupled model discussed in [7], [8] is used to implement the CCS-MPC. When compared to previous work in the area of MMC control for drive applications, the contributions of this work are: 1) The first CCS-MPC algorithm proposed for the control of MMC-based drives is presented and experimentally validated using an 18-cell MMC-based prototype driving a cage machine. It is experimentally shown that two MIMO CCS-MPC algorithms can replace ten or even more SISO controllers typically used in MMC-based drive applications. 2) The implementation of the proposed CCS-MPC is simplified when compared to conventional control systems reported in the literature. For instance, in [6]–[9], the parameters of the circulating currents, such as waveform shape, phase, electrical sequence, frequency, among others, have to be predefined. This is unnecessary and automatically accomplished using the proposed CCS-MPC algorithm. 3) Optimal limitation of the arm currents and voltages in an MMC is easily achieved with CCS-MPC using constraints [24], while it is extremely problematic in a conventional control system [7], [12]; 4) The proposed CCS-MPC algorithm can operate in either LFM or HFM with a seamless optimal transition between modes, in contrast to other control systems reported in [4], [7], [25].

The rest of this paper is organised as it follows. In Section II,

the MMC modelling is briefly described. The MPC formulation to regulate the capacitor voltages and circulating currents are provided in Section III. In Section IV hardware in the loop results are discussed and, in Section V, experimental work is presented. Finally, Section VI presents the conclusions.

## II. MODELLING OF THE MMC

The decoupled model of the MMC discussed in this section has been reported in previous works [4], [8], and for completeness it is briefly addressed here. This work utilises the  $\Sigma\Delta\alpha\beta 0$ -transformation to represent the voltages and currents of the MMC. Using the transformed currents and voltages a simplified decoupled model is obtained (see [4], [8]).

The  $\Sigma\Delta\alpha\beta 0$ -transformation is defined by

$$[X]_{\alpha\beta 0}^{\Sigma\Delta} \doteq [T]_{\Sigma\Delta} \cdot [X]_{abc}^{PN} \cdot [C]_{\alpha\beta 0} \quad (1)$$

Where  $[X]_{abc}^{PN}$  represents the matrix with the instantaneous  $abc$  variables (e.g. capacitor voltages, arm currents, etc.) to be transformed, and the matrices  $[T]_{\Sigma\Delta}$  and  $[C]_{\alpha\beta 0}$  are given by

$$[T]_{\Sigma\Delta} = \begin{bmatrix} \frac{1}{2} & & \\ & \frac{1}{2} & \\ & & -1 \end{bmatrix}, \quad [C]_{\alpha\beta 0} = \begin{bmatrix} \frac{2}{3} & 0 & \frac{1}{3} \\ -\frac{1}{3} & \frac{1}{\sqrt{3}} & \frac{1}{3} \\ -\frac{1}{3} & -\frac{1}{\sqrt{3}} & \frac{1}{3} \end{bmatrix} \quad (2)$$

By applying this transformation to the converter voltages and currents, the dynamics of the MMC can be divided into two models, as shown below. Using the circuit of Fig. 1 and applying Kirchhoff's voltage law, the current-voltage model describing the dynamics of the currents are defined as [10]

$$\frac{V_{dc}}{2} \begin{bmatrix} 1 & 1 & 1 \\ 1 & 1 & 1 \end{bmatrix} = \begin{bmatrix} v_a^P & v_b^P & v_c^P \\ v_a^N & v_b^N & v_c^N \end{bmatrix} + L \frac{d}{dt} \begin{bmatrix} i_a^P & i_b^P & i_c^P \\ i_a^N & i_b^N & i_c^N \end{bmatrix} + \begin{bmatrix} v_a & v_b & v_c \\ -v_a & -v_b & -v_c \end{bmatrix} \quad (3)$$

Then, applying (1) to (3) yields the following transformed model:

$$\frac{1}{2} \begin{bmatrix} 0 & 0 & V_{dc} \\ 0 & 0 & 0 \end{bmatrix} = \begin{bmatrix} v_\alpha^\Sigma & v_\beta^\Sigma & v_0^\Sigma \\ v_\alpha^\Delta & v_\beta^\Delta & v_0^\Delta \end{bmatrix} + L \frac{d}{dt} \begin{bmatrix} i_\alpha^\Sigma & i_\beta^\Sigma & \frac{1}{3}i_{dc} \\ i_\alpha & i_\beta & 0 \end{bmatrix} + 2 \begin{bmatrix} 0 & 0 & 0 \\ v_\alpha & v_\beta & v_0 \end{bmatrix} \quad (4)$$

where  $i_\alpha^\Sigma$  and  $i_\beta^\Sigma$  are the arm circulating currents,  $i_{dc}$  is the DC port current,  $v_0$  is the common-mode voltage and  $v_\alpha$ ,  $v_\beta$ ,  $i_\alpha$  and  $i_\beta$  are the machine voltages and currents. These variables are expressed in  $\alpha\beta 0$ -coordinates.

The instantaneous cluster power can be obtained by using the voltages and currents [8], [9], i.e.,  $p_i^j = v_i^j i_i^j \forall i \in \{a, b, c\}$  and  $j \in \{P, N\}$ . Assuming that the capacitor voltages are close to the reference  $\bar{v}_C^*$ , this power is related to the voltage of the capacitors using the approximation:

$$\frac{d}{dt} \begin{bmatrix} v_{C_a}^P & v_{C_b}^P & v_{C_c}^P \\ v_{C_a}^N & v_{C_b}^N & v_{C_c}^N \end{bmatrix} \approx \frac{1}{nC\bar{v}_C^*} \begin{bmatrix} p_a^P & p_b^P & p_c^P \\ p_a^N & p_b^N & p_c^N \end{bmatrix} \quad (5)$$

where  $n$  is the number of capacitors per cluster,  $C$  is the capacitance of each submodule and  $v_{C_a}^P$ ,  $v_{C_b}^P$ , etc., are the capacitor voltages. Applying the  $\Sigma\Delta\alpha\beta 0$ -transformation to the power-voltage model of (5) yields,

$$\frac{d}{dt} \begin{bmatrix} v_{C_\alpha}^\Sigma & v_{C_\beta}^\Sigma & v_{C_0}^\Sigma \\ v_{C_\alpha}^\Delta & v_{C_\beta}^\Delta & v_{C_0}^\Delta \end{bmatrix} \approx \frac{1}{nC\bar{v}_C^*} \begin{bmatrix} p_\alpha^\Sigma & p_\beta^\Sigma & p_0^\Sigma \\ p_\alpha^\Delta & p_\beta^\Delta & p_0^\Delta \end{bmatrix} \quad (6)$$



$$\begin{aligned}
 \underbrace{\begin{bmatrix} v_{C\alpha}^{\Delta}(k+1) \\ v_{C\beta}^{\Delta}(k+1) \\ v_{C0}^{\Delta}(k+1) \\ v_{\Sigma\alpha}^{\Sigma}(k+1) \\ v_{\Sigma\beta}^{\Sigma}(k+1) \end{bmatrix}}_{\mathbf{x}_{k+1}} &\approx \underbrace{\begin{bmatrix} 1 & 0 & 0 & 0 & 0 \\ 0 & 1 & 0 & 0 & 0 \\ 0 & 0 & 1 & 0 & 0 \\ 0 & 0 & 0 & 1 & 0 \\ 0 & 0 & 0 & 0 & 1 \end{bmatrix}}_{\mathbf{A}} \underbrace{\begin{bmatrix} v_{C\alpha}^{\Delta}(k) \\ v_{C\beta}^{\Delta}(k) \\ v_{C0}^{\Delta}(k) \\ v_{\Sigma\alpha}^{\Sigma}(k) \\ v_{\Sigma\beta}^{\Sigma}(k) \end{bmatrix}}_{\mathbf{x}_k} \\
 &+ K \underbrace{\begin{bmatrix} -v_{\alpha}(k) - 2v_0(k) & v_{\beta}(k) \\ v_{\beta}(k) & v_{\alpha}(k) - 2v_0(k) \\ -v_{\alpha}(k) & -v_{\beta}(k) \\ \frac{1}{2}V_{dc} & 0 \\ 0 & \frac{1}{2}V_{dc} \end{bmatrix}}_{\mathbf{B}} \underbrace{\begin{bmatrix} i_{\alpha}^{\Sigma}(k) \\ i_{\beta}^{\Sigma}(k) \end{bmatrix}}_{\mathbf{u}_k} \\
 &+ K \underbrace{\begin{bmatrix} \frac{1}{2}V_{dc}i_{\alpha}(k) - \frac{2}{3}i_{dc}(k)v_{\alpha}(k) \\ \frac{1}{2}V_{dc}i_{\beta}(k) - \frac{2}{3}i_{dc}(k)v_{\beta}(k) \\ -\frac{2}{3}i_{dc}(k)v_0(k) \\ \frac{1}{4}i_{\beta}(k)v_{\beta}(k) - \frac{1}{4}i_{\alpha}(k)v_{\alpha}(k) - \frac{1}{2}i_{\alpha}(k)v_0(k) \\ \frac{1}{4}i_{\beta}(k)v_{\alpha}(k) + \frac{1}{4}i_{\alpha}(k)v_{\beta}(k) - \frac{1}{2}i_{\beta}(k)v_0(k) \end{bmatrix}}_{\mathbf{d}_k} \quad (9)
 \end{aligned}$$

Using (9) the discrete state space equations can be written as

$$\mathbf{x}_{k+1} = \mathbf{A}\mathbf{x}_k + \mathbf{B}\mathbf{u}_k + \mathbf{d}_k \quad (10)$$

The one-step delay compensation algorithm presented in [33] is applied to (10). The formulation of the outer CCS-MPC stage is given by:

$$\begin{aligned}
 \min_{\mathbf{x}_{k+1}, \mathbf{u}_k} \quad & \mathbf{x}_{k+1}^T \mathbf{Q} \mathbf{x}_{k+1} + \mathbf{u}_k^T \mathbf{R} \mathbf{u}_k \\
 \text{s.t.} \quad & \mathbf{x}_{k+1} = \mathbf{A}\mathbf{x}_k + \mathbf{B}\mathbf{u}_k + \mathbf{d}_k \\
 & \mathbf{G}\mathbf{u}_k \geq \mathbf{W}
 \end{aligned} \quad (11)$$

where  $\mathbf{x}_k$  is the state vector measured at time instant  $k$ ,  $\mathbf{x}_{k+1}$  are the prediction of the state vector at time  $k+1$ , and  $\mathbf{u}_k$  is the control vector.  $\mathbf{A}$  is the system matrix,  $\mathbf{B}$  is the input matrix, and  $\mathbf{Q}$ ,  $\mathbf{R}$  are the weighting matrices that penalise the states and control actions, respectively. Finally,  $\mathbf{d}_k$  represents the set of measurable disturbances in the system, and  $\mathbf{G}$ ,  $\mathbf{W}$  are the constraints imposed on the control actions. The weighting matrices are diagonal and defined as:

$$\mathbf{Q} = \text{Diag}[\lambda_{\alpha}^{\Delta}, \lambda_{\beta}^{\Delta}, \lambda_0^{\Delta}, \lambda_{\alpha}^{\Sigma}, \lambda_{\beta}^{\Sigma}], \quad \mathbf{R} = \text{Diag}[\lambda_{\alpha}^U, \lambda_{\beta}^U] \quad (12)$$

In this work matrices  $\mathbf{Q}$  and  $\mathbf{R}$  are both positive definite and, for LFM operation, the weighting factors  $\lambda_{\alpha}^{\Delta}$  and  $\lambda_{\beta}^{\Delta}$  are modified online as a function of the magnitude of the capacitor voltage oscillations (see the block labelled “weighting factor adaptor” in Fig. 2). This approach is further discussed in Section III-B. The remaining weighting factors are defined as 1.

To simplify the optimal problem [11], [12], [19], the equality constraint of (11) is included in the cost function, yielding:

$$\begin{aligned}
 \min_{\mathbf{u}_k} \quad & \mathbf{u}_k^T \mathbf{H} \mathbf{u}_k + 2 \left[ (\mathbf{A}\mathbf{x}_k + \mathbf{d}_k)^T \mathbf{F} \right] \mathbf{u}_k \\
 \text{s.t.} \quad & \mathbf{G}\mathbf{u}_k \geq \mathbf{W}
 \end{aligned} \quad (13)$$

where

$$\begin{aligned}
 \mathbf{H} &= \mathbf{B}^T \mathbf{Q} \mathbf{B} + \mathbf{R} \\
 \mathbf{F} &= \mathbf{Q} \mathbf{B}
 \end{aligned} \quad (14)$$

Solving (13) (by implementing the active-set method in the control platform), the optimal circulating current vector  $i_{\alpha\beta}^{\Sigma}$

is obtained. Matrices  $\mathbf{H}$  and  $\mathbf{F}$  have to be updated at each sampling time since the system is time variant. Notice that in (9), the common-mode voltage is included as a disturbance. For LFM operation, the optimal circulating currents are automatically obtained by solving (13) and considering  $v_0$ . Notice that the pre-definition of circulating current frequency, waveform shapes, phase shifts and sub-component sequences is no longer required. This feature is one of the important contributions of this paper and it is also applicable to HFM operation.

For saturation limitation to the cluster currents, the circulating currents are limited to  $\pm i_{max}$  by the CCS-MPC outer stage; the value of  $i_{max}$  is selected considering the thermal limits of the MMC devices and components (see [12]). To perform this limitation, the cluster currents are defined in  $\Sigma\Delta\alpha\beta 0$  coordinates as:

$$\begin{bmatrix} i_a^P \\ i_b^P \\ i_c^P \\ i_a^N \\ i_b^N \\ i_c^N \end{bmatrix} = \begin{bmatrix} \frac{1}{3}i_{dc} + \frac{1}{2}i_{\alpha} + i_{\alpha}^{\Sigma} \\ \frac{1}{3}i_{dc} - \frac{1}{4}i_{\alpha} - \frac{1}{2}i_{\alpha}^{\Sigma} + \frac{\sqrt{3}}{2}i_{\beta}^{\Sigma} + \frac{\sqrt{3}}{4}i_{\beta} \\ \frac{1}{3}i_{dc} - \frac{1}{4}i_{\alpha} - \frac{1}{2}i_{\alpha}^{\Sigma} - \frac{\sqrt{3}}{2}i_{\beta}^{\Sigma} - \frac{\sqrt{3}}{4}i_{\beta} \\ \frac{1}{3}i_{dc} - \frac{1}{2}i_{\alpha} + i_{\alpha}^{\Sigma} \\ \frac{1}{3}i_{dc} + \frac{1}{4}i_{\alpha} - \frac{1}{2}i_{\alpha}^{\Sigma} + \frac{\sqrt{3}}{2}i_{\beta}^{\Sigma} - \frac{\sqrt{3}}{4}i_{\beta} \\ \frac{1}{3}i_{dc} + \frac{1}{4}i_{\alpha} - \frac{1}{2}i_{\alpha}^{\Sigma} - \frac{\sqrt{3}}{2}i_{\beta}^{\Sigma} + \frac{\sqrt{3}}{4}i_{\beta} \end{bmatrix} \quad (15)$$

Limiting these currents to  $-i_{max} \leq i_i^j \leq i_{max} \forall i \in \{a, b, c\}$  and  $j \in \{P, N\}$  produces a total of 12 constraints. However, after analysing (15) the constraints can be reduced to six, by exploiting symmetries in the currents  $i_x^P$  and  $i_x^N$  of phase “ $x$ ”,  $\forall x \in \{a, b, c\}$ . After some manipulation, (16) and (17) are obtained:

$$\underbrace{\begin{bmatrix} -1 \\ \frac{1}{2} \\ \frac{1}{2} \\ 1 \\ -\frac{1}{2} \\ -\frac{1}{2} \end{bmatrix}}_{\mathbf{G}} \begin{bmatrix} i_{\alpha}^{\Sigma}(k) \\ i_{\beta}^{\Sigma}(k) \end{bmatrix} \geq \underbrace{\begin{bmatrix} -i_{max} - \min(i_1, i_4) \\ -i_{max} - \min(i_2, i_5) \\ -i_{max} - \min(i_3, i_6) \\ -i_{max} + \max(i_1, i_4) \\ -i_{max} + \max(i_2, i_5) \\ -i_{max} + \max(i_3, i_6) \end{bmatrix}}_{\mathbf{W}} \quad (16)$$

$$\begin{bmatrix} i_1 \\ i_2 \\ i_3 \\ i_4 \\ i_5 \\ i_6 \end{bmatrix} = \begin{bmatrix} -\frac{1}{3}i_{dc}(k) - \frac{1}{2}i_{\alpha}(k) \\ -\frac{1}{3}i_{dc}(k) + \frac{1}{4}i_{\alpha}(k) - \frac{\sqrt{3}}{4}i_{\beta}(k) \\ -\frac{1}{3}i_{dc}(k) + \frac{1}{4}i_{\alpha}(k) + \frac{\sqrt{3}}{4}i_{\beta}(k) \\ -\frac{1}{3}i_{dc}(k) + \frac{1}{2}i_{\alpha}(k) \\ -\frac{1}{3}i_{dc}(k) - \frac{1}{4}i_{\alpha}(k) + \frac{\sqrt{3}}{4}i_{\beta}(k) \\ -\frac{1}{3}i_{dc}(k) - \frac{1}{4}i_{\alpha}(k) - \frac{\sqrt{3}}{4}i_{\beta}(k) \end{bmatrix} \quad (17)$$

## B. On-Line Adaptation of the Cost Function Weights

The optimal algorithm of (13) is designed to drive the voltage unbalances in the capacitors to zero. However, when the system is operating at LFM, a relatively large circulating current interacting with the common mode voltage  $v_0$  [see (7b)] is required to drive the voltage vector  $v_{C\alpha\beta}^{\Delta}$  to zero. Nevertheless, as discussed in previous publications [6], [7], the converter can perform adequately when the capacitor voltage oscillations are maintained within a band of  $\approx 10\%$  of the reference voltage. To achieve this target a variable weight strategy is proposed and the weights  $\lambda_{\alpha}^{\Delta} = \lambda_{\beta}^{\Delta}$  are obtained from the output of a PI controller (see Fig. 2) which acts on the error between a banded reference  $v_{C_d}^{\Delta*}$  and the peak oscillating voltage obtained from the capacitor voltage measurements [processed using the  $\Sigma\Delta\alpha\beta 0$  transform of (2)].

As discussed in [7], during LFM operation, the voltage  $v_{Cd}^\Delta$  is approximately equal to the peak magnitude of the capacitor voltage oscillations. A complete discussion of the relationship between the voltage fluctuations and  $v_{Cdq}^\Delta$  is presented in [7].

The weighting factor control is implemented in a  $d-q$  frame rotating at the frequency of the AC port ( $\omega_e$ ) and orientated along the voltage vector  $\underline{v}_{C\alpha\beta}^\Delta$ . When the AC-port frequency  $\omega_e$  increases, the voltage oscillations  $\underline{v}_{C\alpha\beta}^\Delta$  naturally decrease due to the filtering effect of the submodule capacitors. This allows the implementation of a simple seamless transition between LFM to HFM and vice versa, i.e. when the weights  $\lambda_{\alpha\beta}^\Delta$  are below a predefined threshold, the system is considered in HFM; therefore, the trapezoidal common-mode voltage  $v_0$  could be reduced or indeed it is no longer required.

### C. Circulating Current Control

In this work, a second inner CCS-MPC stage is proposed to control the circulating currents (see Fig. 2) with the model being obtained from (4). To obtain a discrete-time model of the currents the forward Euler approximation is applied.

$$\underbrace{\begin{bmatrix} i_\alpha^\Sigma(k+1) \\ i_\beta^\Sigma(k+1) \end{bmatrix}}_{\mathbf{x}_{k+1}} = \underbrace{\begin{bmatrix} 1 & 0 \\ 0 & 1 \end{bmatrix}}_{\mathbf{A}} \underbrace{\begin{bmatrix} i_\alpha^\Sigma(k) \\ i_\beta^\Sigma(k) \end{bmatrix}}_{\mathbf{x}_k} + \underbrace{\frac{-T_s}{L} \begin{bmatrix} 1 & 0 \\ 0 & 1 \end{bmatrix}}_{\mathbf{B}} \underbrace{\begin{bmatrix} v_\alpha^\Sigma(k) \\ v_\beta^\Sigma(k) \end{bmatrix}}_{\mathbf{u}_k} \quad (18)$$

The inner CCS-MPC receives a circulating current reference from the output of the outer CCS-MPC stage [see (13)] and minimises the following cost function:

$$\begin{aligned} \min_{\mathbf{x}_{k+1}, \mathbf{u}_k} \quad & (\mathbf{x}_{k+1} - \mathbf{x}^*)^T \mathbf{Q} (\mathbf{x}_{k+1} - \mathbf{x}^*) \\ & + (\mathbf{u}_k - \mathbf{u}^*)^T \mathbf{R} (\mathbf{u}_k - \mathbf{u}^*) \\ \text{s.t.} \quad & \mathbf{x}_{k+1} = \mathbf{A}\mathbf{x}_k + \mathbf{B}\mathbf{u}_k \\ & \mathbf{G}\mathbf{u}_k \geq \mathbf{W} \end{aligned} \quad (19)$$

where  $\mathbf{A}$ ,  $\mathbf{B}$  and  $\mathbf{X}$  are defined in (18);  $\mathbf{x}^*$  is the reference state which is equal to the circulating current reference  $i_{\alpha\beta}^{\Sigma*}$ , and  $\mathbf{u}^*$  is the equilibrium control action that brings the system to  $\mathbf{x}^*$ . Furthermore,  $\mathbf{u}^*$  can be obtained as a function of the reference state by

$$\mathbf{u}^* = \mathbf{B}^{-1}(\mathbf{I} - \mathbf{A})\mathbf{x}^* \quad (20)$$

In this case,  $\mathbf{u}^*$  is zero considering that  $\mathbf{A} = \mathbf{I}$  [see (18)]. More details about the resulting equilibrium point are presented in [19]. Simplifying (19) by including  $\mathbf{x}_{k+1} = \mathbf{A}\mathbf{x}_k + \mathbf{B}\mathbf{u}_k$  in the cost function, yields:

$$\begin{aligned} \min_{\mathbf{u}_k} \quad & \mathbf{u}_k^T \mathbf{H} \mathbf{u}_k + 2 \left[ (\mathbf{A}\mathbf{x}_k - \mathbf{x}^*)^T \mathbf{F} \right] \mathbf{u}_k \\ \text{s.t.} \quad & \mathbf{G}\mathbf{u}_k \geq \mathbf{W} \end{aligned} \quad (21)$$

where  $\mathbf{F}$  and  $\mathbf{H}$  are obtained from (14).

The diagonal matrices  $\mathbf{Q}$  and  $\mathbf{R}$  are  $2 \times 2$ , where  $\mathbf{Q} = \text{Diag}[\lambda_\alpha^{\Sigma'}, \lambda_\beta^{\Sigma'}]$  and  $\mathbf{R} = \text{Diag}[\lambda_\alpha^{U'}, \lambda_\beta^{U'}]$ . As discussed in [19], if the weights of  $\mathbf{R}$  are too small, the CCS-MPC algorithm has a fast dynamic response and high sensitivity to noise (i.e similar to a dead-beat response [19]). Using both  $\mathbf{Q}$  and  $\mathbf{R}$  the CCS-MPC dynamic and steady state responses can be tailored for a particular application.

Equation (21) yields the voltage vector  $\underline{v}_{\alpha\beta}^\Sigma$  that optimises the cost function. Due to hardware limitations, the voltages synthesised by each cluster  $[v_a^P, v_b^P, v_c^P, v_a^N, v_b^N, v_c^N]$  are

bounded between zero up to the maximum voltage achievable without producing over-modulation  $[v_{Ca}^P, v_{Cb}^P, v_{Cc}^P, v_{Ca}^N, v_{Cb}^N, v_{Cc}^N]$ . Using the  $\Sigma\Delta\alpha\beta$  transform, the cluster voltages are obtained as:

$$\begin{bmatrix} v_a^P \\ v_b^P \\ v_c^P \\ v_a^N \\ v_b^N \\ v_c^N \end{bmatrix} = \begin{bmatrix} v_0^\Sigma + \frac{1}{2}v_0^\Delta + \frac{1}{2}v_\alpha^\Delta + v_\alpha^\Sigma \\ v_0^\Sigma + \frac{1}{2}v_0^\Delta - \frac{1}{4}v_\alpha^\Delta - \frac{1}{2}v_\alpha^\Sigma + \frac{\sqrt{3}}{2}v_\beta^\Sigma + \frac{\sqrt{3}}{4}v_\beta^\Delta \\ v_0^\Sigma + \frac{1}{2}v_0^\Delta - \frac{1}{4}v_\alpha^\Delta - \frac{1}{2}v_\alpha^\Sigma - \frac{\sqrt{3}}{2}v_\beta^\Sigma - \frac{\sqrt{3}}{4}v_\beta^\Delta \\ v_0^\Sigma - \frac{1}{2}v_0^\Delta - \frac{1}{2}v_\alpha^\Delta + v_\alpha^\Sigma \\ v_0^\Sigma - \frac{1}{2}v_0^\Delta + \frac{1}{4}v_\alpha^\Delta - \frac{1}{2}v_\alpha^\Sigma + \frac{\sqrt{3}}{2}v_\beta^\Sigma - \frac{\sqrt{3}}{4}v_\beta^\Delta \\ v_0^\Sigma - \frac{1}{2}v_0^\Delta + \frac{1}{4}v_\alpha^\Delta - \frac{1}{2}v_\alpha^\Sigma - \frac{\sqrt{3}}{2}v_\beta^\Sigma + \frac{\sqrt{3}}{4}v_\beta^\Delta \end{bmatrix} \quad (22)$$

Considering the upper and lower limits, (22) represents 12 constraints. Using symmetries in the voltages  $v_x^P$  and  $v_x^N$  of phase " $x$ ",  $\forall x \in \{a, b, c\}$  these 12 constraints can be reduced to 6, yielding:

$$\underbrace{\begin{bmatrix} -1 & 0 \\ \frac{1}{2} & -\frac{\sqrt{3}}{2} \\ \frac{1}{2} & \frac{\sqrt{3}}{2} \\ 1 & 0 \\ -\frac{1}{2} & \frac{\sqrt{3}}{2} \\ -\frac{1}{2} & -\frac{\sqrt{3}}{2} \end{bmatrix}}_{\mathbf{G}} \underbrace{\begin{bmatrix} v_\alpha^\Sigma(k) \\ v_\beta^\Sigma(k) \end{bmatrix}}_{\mathbf{w}} \geq \underbrace{\begin{bmatrix} -\min(v_1 + v_{Ca}^P(k), v_4 + v_{Ca}^N(k)) \\ -\min(v_2 + v_{Cb}^P(k), v_5 + v_{Cb}^N(k)) \\ -\min(v_3 + v_{Cc}^P(k), v_6 + v_{Cc}^N(k)) \\ \max(v_1, v_4) \\ \max(v_2, v_5) \\ \max(v_3, v_6) \end{bmatrix}}_{\mathbf{W}} \quad (23)$$

where

$$\begin{bmatrix} v_1 \\ v_2 \\ v_3 \\ v_4 \\ v_5 \\ v_6 \end{bmatrix} = \begin{bmatrix} -v_0^\Sigma(k) - \frac{1}{2}v_0^\Delta(k) - \frac{1}{2}v_\alpha^\Delta(k) \\ -v_0^\Sigma(k) - \frac{1}{2}v_0^\Delta(k) + \frac{1}{4}v_\alpha^\Delta(k) - \frac{\sqrt{3}}{4}v_\beta^\Delta(k) \\ -v_0^\Sigma(k) - \frac{1}{2}v_0^\Delta(k) + \frac{1}{4}v_\alpha^\Delta(k) + \frac{\sqrt{3}}{4}v_\beta^\Delta(k) \\ -v_0^\Sigma(k) + \frac{1}{2}v_0^\Delta(k) + \frac{1}{2}v_\alpha^\Delta(k) \\ -v_0^\Sigma(k) + \frac{1}{2}v_0^\Delta(k) - \frac{1}{4}v_\alpha^\Delta(k) + \frac{\sqrt{3}}{4}v_\beta^\Delta(k) \\ -v_0^\Sigma(k) + \frac{1}{2}v_0^\Delta(k) - \frac{1}{4}v_\alpha^\Delta(k) - \frac{\sqrt{3}}{4}v_\beta^\Delta(k) \end{bmatrix} \quad (24)$$

Notice that a well designed MMC has an adequate voltage margin to synthesise  $\underline{v}_{\alpha\beta}^\Sigma$  (see [28]); however in case the control action has a very high dynamic response the constraints of (23) are required in (21) to avoid over-modulation during transients.

## IV. HIL AND SIMULATION RESULTS

A HIL platform is used in this section to perform work that requires a good repeatability between tests, or tests that could exceed some ratings in the experimental systems.

### A. System Performance and Constraints Operation for Load Changes

Two PLECS-RT Box-1 HIL platforms are employed to model the MMC and the vector-controlled induction machine with a time step of  $6.5 \mu\text{s}$ . The control system is implemented using a dSPACE MicroLabBox (see more details in Section V). The HIL-model utilises the parameters and weights used in the experimental system (see Table I).

Two tests were performed for an output frequency of  $\approx 4$  Hz ( $\approx 240$  rpm). In every test, a predefined maximum limit was used for the arm currents; additionally, for each test, a torque impact between 0 to  $\approx 60\%$  of the nominal torque is applied to the electrical machine, for  $0.1 \text{ s} \leq t \leq 0.5$  s. Note that  $v_{Cd}^* = 11.25$  V. Fig. 4 shows the experimental results illustrating (from top to bottom) the cluster currents, the machine currents, the circulating currents and the capacitor voltages. The results depicted in Fig. 4(a)-(d) correspond to operation without any current constraints. On the other hand

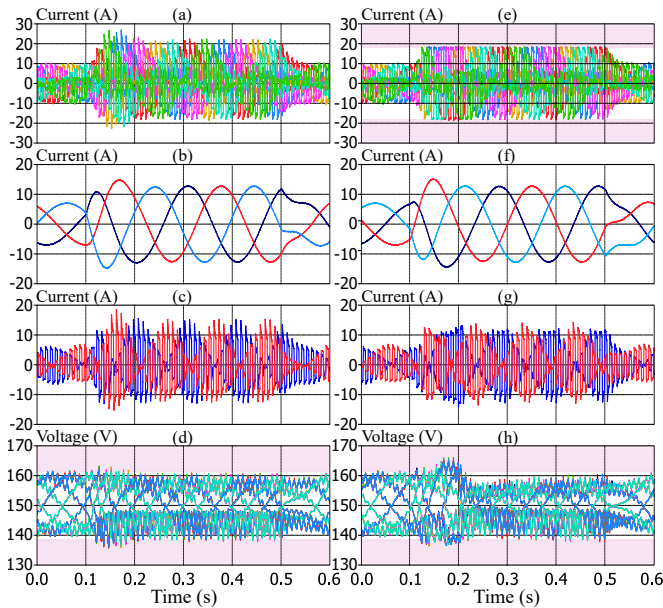


Fig. 4. HIL results of the saturation limitation of the circulating currents to limit the clusters' currents. Left: without saturation, right: 18 A saturation. (a) and (e) Cluster currents  $i_a^P, i_b^P$ , etc. (b) and (f) Machine currents  $i_a, i_b$  and  $i_c$ . (c) and (g) Circulating currents  $i_{\alpha}^{\Sigma}$  and  $i_{\beta}^{\Sigma}$ . (d) and (h) Capacitor voltages  $v_{Ca1}^P, v_{Ca2}^P$ , etc.

Fig. 4(e)-(h) shows the performance of the control system for current limits of 18 A. It should be noted that this 18 A limit is arbitrarily selected, to demonstrate the performance of the constraints in the CCS-MPC algorithm, and do not necessarily reflect nominal ratings. Notice that the step torque transient increases the current in the MMC arms, reducing the margin allowed for the circulating currents. For the unconstrained case of Fig. 4(a)-(d), the total current in the arms has peaks of  $\approx 28$  A. However, regulation of the capacitor voltages is very good with all of them maintained well inside the predefined band. Figs 4(e)-(h) show the performance of the algorithm when the limit of 18 A is enforced. It is illustrated that the limitation is achieved by reducing the circulating currents  $i_{\alpha\beta}^{\Sigma}$  without affecting the induction machine stator currents. The capacitor voltages are slightly affected by the step change in the torque current, however after a fast transient they return to their previous values.

To validate operation with cluster voltage constraints, a trapezoidal  $v_0$  of 202.5 V peak is used; i.e. a relatively high value of  $v_0$  is arbitrarily applied in this test, reducing the voltage margin available for regulating  $i_{\alpha\beta}^{\Sigma*}$  and forcing operation with the constraints in (21) activated. Fig. 5 shows the performance with and without voltage restrictions and with the induction machine operating at 240 rpm ( $\approx 4$  Hz). As before,  $v_{Cd}^{\Delta*} = 11.25$  V (see Fig. 2) and the torque step transient is imposed for  $0.1 \text{ s} \leq t \leq 0.5 \text{ s}$ . From top to bottom, Fig. 5 shows the voltages synthesised by leg A, the  $\alpha$ -axis circulating current, and the machine currents. Additionally, graphs (a), (b), (c) and (d) include the total cluster voltages in red. Without voltage constraints, the peak voltages synthesised by the arms exceed the total cluster voltages, producing over-modulation and some distortion in the machine currents as shown in Fig. 5(g). Conversely, when voltage constraints are included, the

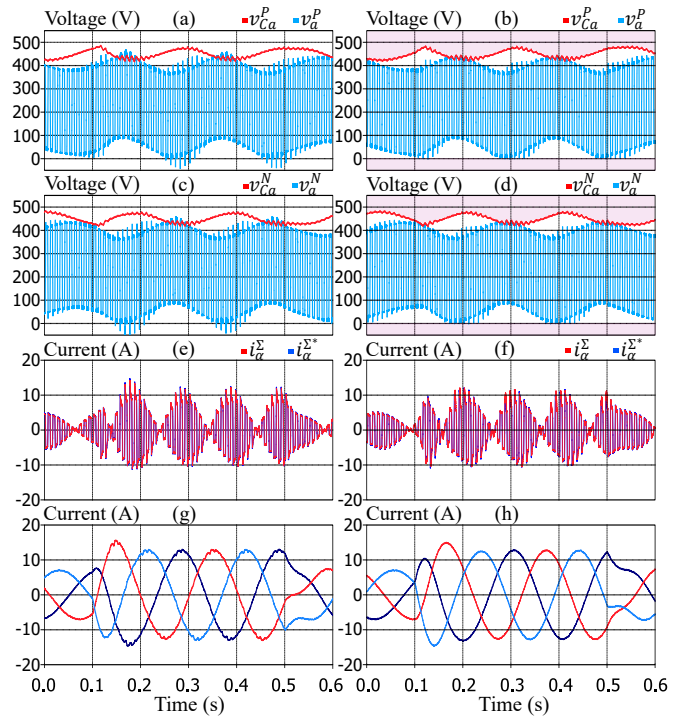


Fig. 5. HIL results of the clusters output voltages with (right) and without (left) saturation limitation. (a)-(b) Total cluster voltage  $v_{Ca}^P$  and cluster output voltage  $v_a^P$ , (c)-(d) total cluster voltage  $v_{Ca}^N$  and cluster output voltage  $v_a^N$ , (e)-(f) circulating current  $i_{\alpha}^{\Sigma}$  and its reference  $i_{\alpha}^{\Sigma*}$ , (g)-(h) machine currents  $i_a, i_b$  and  $i_c$ .

voltages synthesised in the arms are limited by the total cluster voltages as shown in Fig. 5(b) and Fig. 5(d); note that even the low voltage capacitor fluctuations produced in  $v_{Ca}^{PN}$  are considered by the inner-CCS algorithm when synthesising the voltages  $v_a^{PN}$ . However, the voltage limitations of (23), used in the constrained-optimisation problem of (19), limit the control effort of the inner CCS-MPC algorithm. Clearly saturation limitation reduces the tracking performance producing an increased circulating current tracking error ( $i_{\alpha\beta}^{\Sigma*} - i_{\alpha\beta}^{\Sigma}$ ). The dispersion of the circulating current tracking error increases from  $\sigma \approx 0.35$  A (unconstrained case) to  $\sigma \approx 0.75$  A (constrained case). Nevertheless, Fig. 5(b) and Fig. 5(d) show that the capacitor voltages are relatively well regulated, with voltage fluctuations comparable to those obtained for the unconstrained case. When the constraints are enabled, the machine current THD [see Fig. 5(h)] is  $\approx 0.5\%$  whereas, for the case without constraints [see Fig.5(g)], the THD increases to 1.8% due to over-modulation.

### B. Performance Comparison of Conventional SISO-Based Control System and Proposed two-stage CCS-MPC

The performance of the proposed CCS-MPC is compared to that obtained by the SISO-based control system discussed in [7]. For both cases it is assumed that the machine stator frequency is 1.7 Hz ( $\approx 100$  rpm). The results are shown in Fig. 6 with the CCS-MPC results being shown at the right. The SISO-based control system also includes an allowable capacitor-voltage oscillation band. The same operating conditions and common-mode voltage are used to perform a fair comparison.

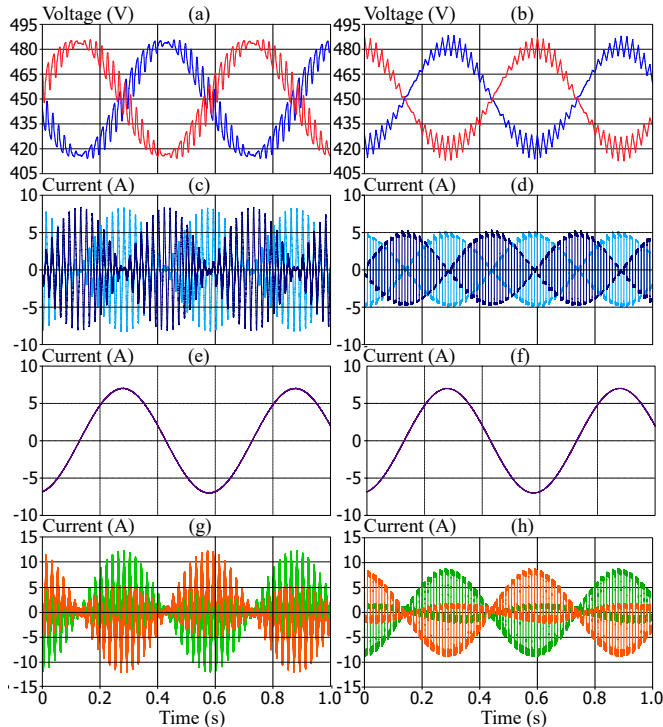


Fig. 6. MMC static performance at LFM using multiple SISO control loops (left) and proposed two-stage CCS-MPC (right). (a)-(b) Total cluster voltages  $v_{Ca}^P$  and  $v_{Ca}^N$ , (c)-(d) Circulating currents  $i_{\alpha}^{\Sigma}$  and  $i_{\beta}^{\Sigma}$ , (e)-(f) Machine current  $i_a$ , (g)-(h) Cluster currents  $i_a^P$  and  $i_a^N$ .

When analysing Fig. 6, the advantages of using the CCS-MPC strategy are clear. The proposed controller significantly reduces the peak circulating currents at this operating point [see Fig. 6(c)-(d)] and also reduces the cluster currents by 30%. This improvement is due to the much faster dynamic response and higher bandwidth of the predictive controller, and the fact that the shape, frequency, phase and sequence of the circulating currents are automatically and optimally adjusted by the CCS-MPC algorithm of (13). According to the results obtained here, the circulating current component, which interacts with  $v_0$  in the term  $2v_0i_{\alpha\beta}^{\Sigma}$  of (7b), has a lower peak than that produced by the SISO implementation proposed in [7] because the CCS-MPC can generate trapezoidal waveforms in the circulating currents allowing for reduced semiconductor current stress. The reduction in the peak circulating currents during LFM could improve the converter efficiency in this operating mode. However, efficiency studies are considered outside the scope of this work. The effects of trapezoidal circulating currents on semiconductor current ratings and capacitor dimensioning are discussed in [25].

As mentioned before, it should be noted that the scheme proposed in [7] does not include globally managed constraints on the circulating currents, unlike the proposed CCS-MPC. Therefore to limit the cluster currents, conventional anti-windup schemes are considered in the SISO-implemented PIs and resonant controllers. Moreover, as stated before, optimal saturation is not simple to achieve in SISO control of MMC. In [7], the circulating currents are regulated by seven independent PI controllers instead of a single MIMO controller. Implementing seven anti-windup schemes to limit the output currents of seven PI controllers leads to sub-optimal solutions (see [12]), compared to those achieved by the CCS-MPC algorithms. This

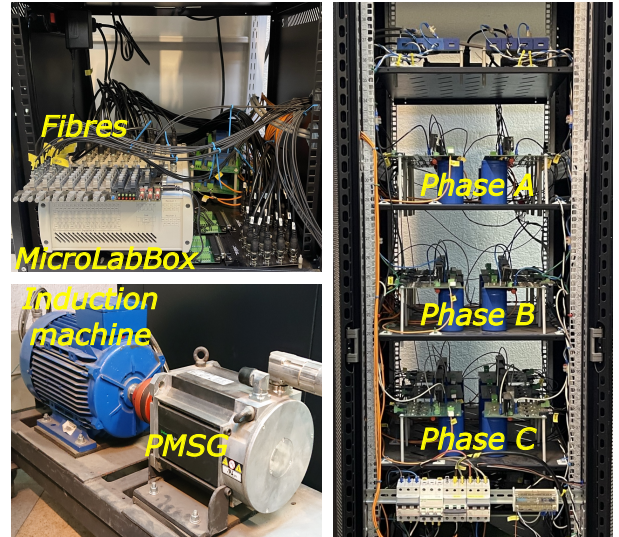


Fig. 7. Experimental system. At the top left is the dSPACE MicroLabBox connected to an optical-fibre interface board. At the bottom left is the cage machine driving a PMSG. At the right is the 18-cell MMC prototype.

is further discussed in Section I and demonstrated in [12].

## V. EXPERIMENTAL RESULTS

Validation of the proposed control scheme is performed using the MMC-based motor drive prototype shown in Fig. 7, whose parameters are given in Table I. As mentioned in Section III-A, the weighting factors used in the outer controller are unity (i.e.,  $\lambda_0^{\Delta} = \lambda_{\alpha}^{\Sigma} = \lambda_{\beta}^{\Sigma} = \lambda_{\alpha}^U = \lambda_{\beta}^U = 1$ ) except for  $\lambda_{\alpha}^{\Delta}$  and  $\lambda_{\beta}^{\Delta}$ , which are the only ones adjusted by the weighting factor controller (see Section III-B). On the other hand, the weighting factors used in the inner controller are  $\lambda_{\alpha'}^{\Sigma'} = \lambda_{\beta'}^{\Sigma'} = 1$  and  $\lambda_{\alpha'}^U = \lambda_{\beta'}^U = 1 \times 10^{-3}$ . To control the system, a dSPACE MicroLabBox platform is used, which is composed of a Freescale QorIQ P5020 dual-core 2 GHz processor and a Xilinx Kintex-7 XC7K325T FPGA. In this implementation, the FPGA performs an In-Phase Carrier Disposition (IPD-PWM) modulation scheme and a sorting algorithm. At the same time, the processor executes the optimisations, the active-set solver and the remaining control algorithms. The control platform includes 32 parallel ADCs that are used to simultaneously perform and store all the measurements into FPGA registers.

The MMC drives a 7.5 kW vector-controlled induction machine connected to a permanent magnet synchronous generator (PMSG). A resistor bank has been connected to the PMSG output to provide an electrical load. Hall effect transducers are used to measure the capacitor voltages and cluster currents. A 10,000 ppr position encoder is fixed to the machine shaft. 18 optical-fibre links transmit the switching signals from the control platform to the gate drivers of the MOSFET switches (model IXFH72N30X3, nominal ratings of 72 A, 300 V, 15 mΩ On-Resistance). For the 10 kHz switching frequency, a sampling time of 50 μs is used for the implementation of the control algorithms.

### A. Dynamic Performance of the Control Strategy

Validation of the dynamic performance of the proposed CCS-MPC strategy is tested over a large operating speed

TABLE I  
 MMC AND INDUCTION MACHINE PARAMETERS

Symbol	Parameter	Value	Unit
$C$	Submodule capacitance	2,200	$\mu\text{F}$
$L$	Cluster inductance	2.5	mH
$\bar{v}_C^*$	Submodules DC voltage	150	V
$n$	Submodules per cluster	3	-
$f_s$	Carrier frequency	10	kHz
$V_{dc}$	DC port voltage	450	V
$P$	Power	7.5	kW
$V_m$	Machine rms voltage	380	V
$f$	Frequency	50	Hz
$p$	Pole number	2	-
$R_s/R_r$	Stator/rotor resistances	367/533	m $\Omega$
$L_s/L_r/L_m$	Stator/Rotor/Mutual inductances	139/139/135	mH

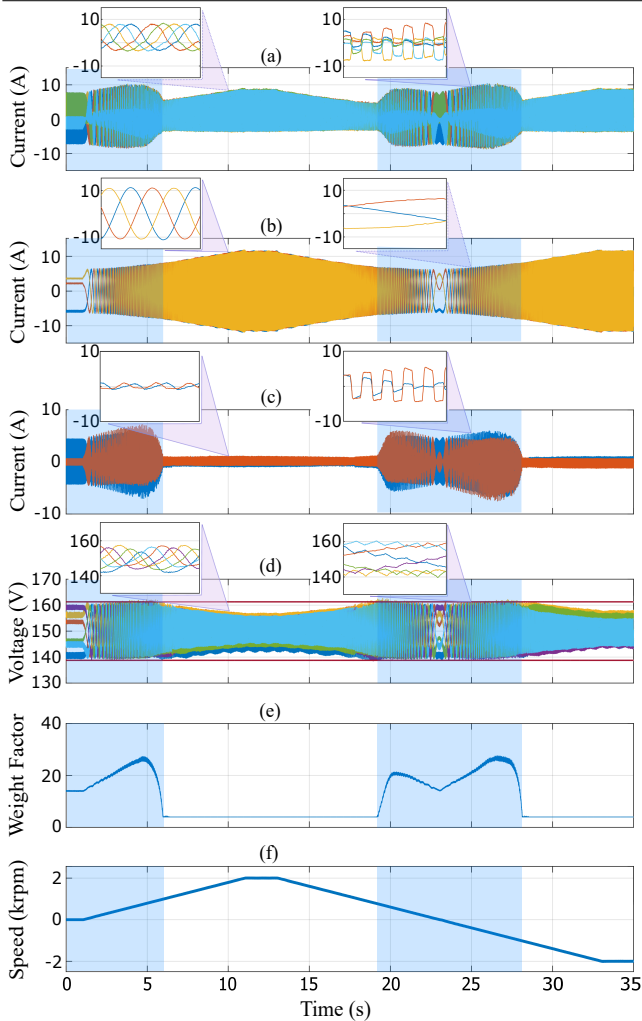


Fig. 8. System response to a ramp speed variation. (a) Cluster currents  $i_a^P, i_b^P, \dots$ , (b) Machine currents  $i_a, i_b$  and  $i_c$ , (c) Circulating currents  $i_{\alpha}^{\Sigma}$  and  $i_{\beta}^{\Sigma}$ , (d) Capacitor voltages  $v_{Ca1}^P, v_{Ca2}^P, \dots$ , (e) Weighting factors  $\lambda_{\alpha}^{\Delta}$  and  $\lambda_{\beta}^{\Delta}$ , and (f) Machine speed  $\omega_r$ . The zoom-in on the time axis is performed at  $t = 10$  s (HFM) and  $t = 25$  s (LFM) with a time interval of 50 ms for both cases.

range, including operation at standstill ( $\omega_e = 0$ ). Fig. 8 shows the experimental results, where a zoom-in on the capacitor voltages and converter currents at LFM and HFM is provided for Figs 8(a)-(d). In this test the different operating regions and the behaviour of the system for the LFM-HFM transition can be observed. A tolerance band of  $v_{Cd}^{\Delta*} = 11.25$  V (see Fig.

2), which represents 7.5% of the capacitor voltage reference  $\bar{v}_C^*$ , is used in the variable weight strategy and is illustrated in Fig. 8(d) by the red lines. The low-frequency region, where the control strategy operates in LFM, is indicated by a blue band. As shown in Fig. 8(d), the capacitor voltages are maintained inside the 7.5% tolerance bounds even when the machine operates at a very low frequency during the initial start-up. Notice that during HFM all the capacitor voltages remain well inside the predefined band even when all the  $\lambda_{\alpha\beta}^{\Delta}$  are adjusted to the minimum value.

In Fig. 8(e) the weighting variations  $\lambda_{\alpha}^{\Delta}$  and  $\lambda_{\beta}^{\Delta}$  are analysed. Initially, the weights have a relatively high value because the machine is at standstill with only the magnetising current  $i_d$  applied to the stator (i.e. LFM operation with  $\omega_e \approx 0$ ). At  $t = 0$ , when the torque current is applied, the weighting factors increase [see Figs. 8(b) and (e)]. However, when the AC-port frequency is relatively large, the capacitor filtering effect naturally reduces the voltage oscillations. Consequently, the values of the weighting factors [see Fig. 8(e)], circulating currents [see Fig. 8(c)] and total arm currents [see Fig. 8(a)] are also reduced. Moreover, during HFM and in steady state operation ( $12 \text{ s} < t < 12.03 \text{ s}$ ), the THD is only 0.7%. Regulation of the weighting factors to maintain the capacitor voltages inside a predefined band also allows a seamless transition between LFM and HFM as depicted in Fig. 8(e) for  $t < 6$  s and between  $19.2 \text{ s} < t < 28.1 \text{ s}$ . This is also shown in the scope shot of Fig. 9 where an amplified view of the transition between LFM to HFM is depicted. When the weighting factors are reduced from a peak-value of  $\approx 30$  to  $\approx 4$  the trapezoidal common-mode voltage is eliminated and the HFM mode is enabled.

Notice that the proposed methodology is different to that reported in some previous publications (see [4], [6], [10]), where a stator frequency value ( $\omega_e$ ) is used as a hard limit between LFM and HFM, e.g.  $\omega_e = 12$  Hz [6] that is enforced regardless of the magnitudes of the circulating currents and capacitor voltage oscillations. Additionally, the optimal algorithm of (13) automatically adjusts all the circulating current parameters to optimise the cost function as shown in Fig. 10. The top waveform corresponds to the common mode voltage and the medium and bottom waveforms correspond to the circulating currents  $i_{\alpha}^{\Sigma}$  and  $i_{\beta}^{\Sigma}$  respectively. Here the machine is operating with a stator frequency of  $\approx 4$  Hz (i.e. LFM operation), and a stator current of 5 A.

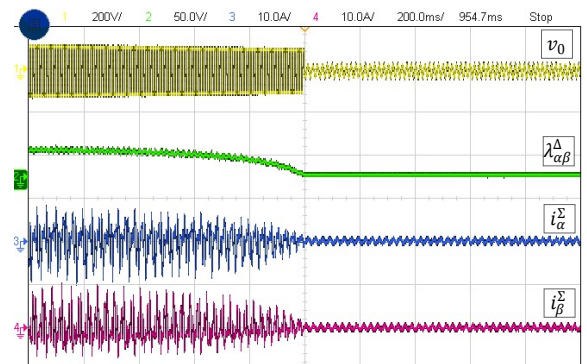


Fig. 9. Transition region from LFM to HFM. Yellow: common-mode voltage, green: weighting factors, blue and red: circulating currents.

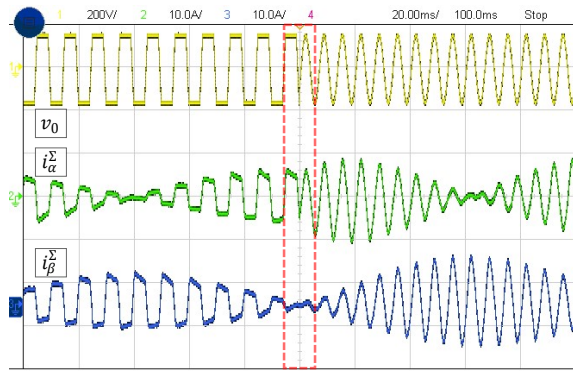


Fig. 10. Experimental results obtained for an online "on the fly" change of the waveform shape and frequency of the common-mode voltage. Yellow: common-mode voltage, green and blue: circulating currents.

In Fig. 10, for  $0 \leq t < 100$  ms a trapezoidal 100 Hz waveform for  $v_0$  is used. This waveform is changed to a 150 Hz sinusoidal waveform by the control algorithm for  $100 \text{ ms} \leq t \leq 200$  ms. It can be observed that these circulating current components, obtained from (19), (21), automatically adopt the same phase shift, frequency and waveform shape as the common mode voltage, confirming that predefinition of circulating current parameters is not required in the proposed algorithm. As shown in Fig. 10, for a sinusoidal  $v_0$  the circulating current peak value is increased.

Additionally, the execution time was measured during the test shown in Fig. 8. This computation time includes the analogue-to-digital conversions and all calculations performed by the QorIQ P5020 processor. The maximum execution time obtained during the test was  $15.8 \mu\text{s}$ , which represents 31.6% of the total sampling period. Note that the optimisation problems described in Sections III-A and III-C do not depend on the number of converter submodules. Therefore, as aforementioned, the computational complexity of the two-stage CCS-MPC does not depend on the number of submodules per cluster, unlike most strategies based on FCS-MPC [5]. In addition, it should be noted that the sorting algorithm can be efficiently implemented in the FPGA taking advantage of its parallel computing capabilities [17]. For example, the modulation and sorting algorithms are executed in less than 10 ns for this implementation. Moreover, to further investigate the computational burden, the conventional SISO strategy proposed in [7] was implemented. The execution time obtained for this control proposal was  $14.9 \mu\text{s}$ . Although the computational burden of the algorithm presented in [7] is lower, this difference is negligible, less than  $1 \mu\text{s}$ , or about 1.8% of the time period available.

## VI. CONCLUSIONS

This paper has presented a two-stage CCS-MPC strategy for regulating the capacitor voltages and the circulating currents of MMC-based drives. As discussed in this paper, saturation of voltages and currents are important tasks which are very difficult to address using conventional linear controllers considering that, in a typical MMC-based drive, each cluster current may have components of several frequencies and positive and negative sequences. However, saturation of voltages and currents are simple to achieve using the proposed CCS-MPC methodology where the maximum currents allowed in

each cluster can be considered as constraints as well as the maximum voltage to be synthesised without producing over-modulation. To solve the intrinsic optimisation problem formulated from the MPC, an Active-Set algorithm, implemented in the dSPACE MicroLabBox, has been integrated into the proposed control methodology.

An important feature of the proposed CCS-MPC, is design simplicity because MMC-based drives are MIMO converters. Therefore, to design the control systems using a MIMO-design approach has advantages over the conventional approach of utilising many SISO designed controllers which are implemented considering simplified models where most of the cross-couplings between the different state variables are neglected. Moreover, for the proposed CCS-MPC algorithm the predefinition of the waveform shape, frequency, electrical sequences, and even phase shifts for the circulating currents are not necessary; all these parameters are automatically obtained when solving the constrained-optimisation methodology proposed in this work. Additionally, the circulating current is optimal and, according to the results obtained in this research effort, for the same common-mode voltage and during LFM operation, the peak values of the circulating currents are usually lower than that obtained using conventional control systems. The effects of the proposed CCS-MPC, in the efficiency achieved at LFM operation, will be addressed in a future work.

The experimental results presented in this work shows the high performance and good dynamic performance achieved by the proposed two-stage CCS-MPC algorithm for both, LFM and HFM operation. Moreover, a seamless transition between LFM to HFM operation and vice versa, has been achieved with the proposed control method.

## REFERENCES

- [1] A. Lesnicar and R. Marquardt, "An innovative modular multilevel converter topology suitable for a wide power range," in *2003 IEEE Bologna PowerTech - Conference Proceedings*, vol. 3, pp. 6–11, 2003.
- [2] M. A. Perez, S. Bernet, J. Rodriguez, S. Kouro, and R. Lizana, "Circuit Topologies, Modeling, Control Schemes, and Applications of Modular Multilevel Converters," *IEEE Transactions on Power Electronics*, vol. 30, no. 1, pp. 4–17, 1 2015.
- [3] A. Dekka, B. Wu, R. L. Fuentes, M. Perez, and N. R. Zargari, "Evolution of Topologies, Modeling, Control Schemes, and Applications of Modular Multilevel Converters," *IEEE Journal of Emerging and Selected Topics in Power Electronics*, vol. 5, no. 4, pp. 1631–1656, Dec. 2017.
- [4] M. Espinoza, R. Cárdenas, M. Díaz, and J. C. Clare, "An Enhanced dq-Based Vector Control System for Modular Multilevel Converters Feeding Variable-Speed Drives," *IEEE Transactions on Industrial Electronics*, vol. 64, no. 4, pp. 2620–2630, Apr. 2017.
- [5] A. Dekka, B. Wu, V. Yaramasu, R. L. Fuentes, and N. R. Zargari, "Model Predictive Control of High-Power Modular Multilevel Converters - An Overview," *IEEE Journal of Emerging and Selected Topics in Power Electronics*, vol. 7, no. 1, pp. 168–183, Mar. 2019.
- [6] M. Hagiwara, I. Hasegawa, and H. Akagi, "Start-up and low-speed operation of an electric motor driven by a modular multilevel cascade inverter," *IEEE Transactions on Industry Applications*, vol. 49, no. 4, pp. 1556–1565, 2013.
- [7] M. Espinoza-B, R. Cardenas, J. Clare, D. Soto-Sanchez, M. Diaz, E. Espina, and C. M. Hackl, "An integrated converter and machine control system for MMC-based high-power drives," *IEEE Transactions on Industrial Electronics*, vol. 66, no. 3, pp. 2343–2354, Mar. 2019.
- [8] F. Kammerer, M. Gommeringer, J. Kolb, and M. Braun, "Energy balancing of the modular multilevel matrix converter based on a new transformed arm power analysis," in *2014 16th European Conference on Power Electronics and Applications*, pp. 1–10, Aug. 2014.
- [9] M. Hagiwara, K. Nishimura, and H. Akagi, "A medium-voltage motor drive with a modular multilevel pwm inverter," *IEEE Transactions on Power Electronics*, vol. 25, no. 7, pp. 1786–1799, Jul. 2010.

- [10] J. Kolb, F. Kammerer, M. Gommeringer, and M. Braun, "Cascaded control system of the modular multilevel converter for feeding variable-speed drives," *IEEE Transactions on Power Electronics*, vol. 30, no. 1, pp. 349–357, 2015.
- [11] T. Geyer, *Model predictive control of high power converters and industrial drives*, 1st ed. Wiley & Sons, 2016.
- [12] M. Urrutia, R. Cardenas, J. Clare, and A. Watson, "Circulating Current Control for the Modular Multilevel Matrix Converter Based on Model Predictive Control," *IEEE Journal of Emerging and Selected Topics in Power Electronics*, vol. 9, no. 5, pp. 6069–6085, Oct. 2021.
- [13] M. Espinoza, R. Cárdenas, M. Díaz, A. Mora, and D. Soto, "Modelling and control of the modular multilevel converter in back to back configuration for high power induction machine drives," in *IECON 2016 - 42nd Annual Conference of the IEEE Industrial Electronics Society*, pp. 5046–5051, Oct. 2016.
- [14] P. Münch, D. Görge, M. Izák, and S. Liu, "Integrated current control, energy control and energy balancing of modular multilevel converters," in *IECON 2010 - 36th Annual Conference on IEEE Industrial Electronics Society*, pp. 150–155, 2010.
- [15] S. Fuchs, M. Jeong, and J. Biela, "Long Horizon, Quadratic Programming Based Model Predictive Control (MPC) for Grid Connected Modular Multilevel Converters (MMC)," *IECON Proceedings (Industrial Electronics Conference)*, pp. 1805–1812, 2019.
- [16] S. Kouro, M. A. Perez, J. Rodríguez, A. M. Llor, and H. A. Young, "Model predictive control: Mpc's role in the evolution of power electronics," *IEEE Industrial Electronics Magazine*, vol. 9, no. 4, pp. 8–21, Dec. 2015.
- [17] A. Mora, M. Urrutia, R. Cárdenas, A. Angulo, M. Espinoza, M. Díaz, and P. Lezana, "Model-predictive-control-based capacitor voltage balancing strategies for modular multilevel converters," *IEEE Transactions on Industrial Electronics*, vol. 66, no. 3, pp. 2432–2443, 2019.
- [18] S. Du, A. Dekka, B. Wu, and N. Zargari, *Modular multilevel converters: analysis, control, and applications*. John Wiley & Sons, Jan. 2018.
- [19] D. E. Quevedo, R. P. Aguilera, and T. Geyer, *Predictive Control in Power Electronics and Drives: Basic Concepts, Theory, and Methods*, ch. 5, pp. 181–226. Cham: Springer International Publishing, 2014.
- [20] P. Liu, Y. Wang, W. Cong, and W. Lei, "Grouping-sorting-optimized model predictive control for modular multilevel converter with reduced computational load," *IEEE Transactions on Power Electronics*, vol. 31, no. 3, pp. 1896–1907, Mar. 2016.
- [21] P. Guo, Z. He, Y. Yue, Q. Xu, X. Huang, Y. Chen, and A. Luo, "A novel two-stage model predictive control for modular multilevel converter with reduced computation," *IEEE Transactions on Industrial Electronics*, vol. 66, no. 3, pp. 2410–2422, Mar. 2019.
- [22] J. Yin, J. I. Leon, M. A. Perez, L. G. Franquelo, A. Marquez, and S. Vazquez, "Model predictive control of modular multilevel converters using quadratic programming," *IEEE Transactions on Power Electronics*, vol. 36, no. 6, pp. 7012–7025, Jun. 2021.
- [23] J. Wang, X. Liu, Q. Xiao, D. Zhou, H. Qiu, and Y. Tang, "Modulated model predictive control for modular multilevel converters with easy implementation and enhanced steady-state performance," *IEEE Transactions on Power Electronics*, vol. 35, no. 9, pp. 9107–9118, Sep. 2020.
- [24] J. Nocedal and S. Wright, *Numerical Optimization*, 2nd ed. New York, NY: Springer, 2006.
- [25] B. Li, S. Zhou, D. Xu, R. Yang, D. Xu, C. Buccella, and C. Cecati, "An Improved Circulating Current Injection Method for Modular Multilevel Converters in Variable-Speed Drives," *IEEE Transactions on Industrial Electronics*, vol. 63, no. 11, pp. 7215–7225, Nov. 2016.
- [26] B. Li, S. Zhou, D. Xu, D. Xu, and W. Wang, "Comparative study of the sinusoidal-wave and square-wave circulating current injection methods for low-frequency operation of the modular multilevel converters," in *2015 IEEE Energy Conversion Congress and Exposition (ECCE)*, DOI 10.1109/ECCE.2015.7310324, pp. 4700–4705, 2015.
- [27] J. Xu, C. Zhao, Y. Xiong, C. Li, Y. Ji, and T. An, "Optimal design of mmc levels for electromagnetic transient studies of mmc-hvdc," *IEEE Transactions on Power Delivery*, vol. 31, no. 4, pp. 1663–1672, 2016.
- [28] C. Oates, "Modular multilevel converter design for vsc hvdc applications," *IEEE Journal of Emerging and Selected Topics in Power Electronics*, vol. 3, no. 2, pp. 505–515, 2015.
- [29] H. J. Ferreau, H. G. Bock, and M. Diehl, "An online active set strategy to overcome the limitations of explicit mpc," *International Journal of Robust and Nonlinear Control*, vol. 18, no. 8, pp. 816–830, 2008.
- [30] G. Cimini, D. Bernardini, S. Levijoki, and A. Bemporad, "Embedded model predictive control with certified real-time optimization for synthesis methods for quadratic programming," *IEEE Transactions on Automatic Control*, vol. 62, no. 12, pp. 6094–6109, 2017.

- chronous motors," *IEEE Transactions on Control Systems Technology*, vol. 29, no. 2, pp. 893–900, 2021.
- [32] B. Kouvaritakis and M. Cannon, *Model Predictive Control: Classical, Robust and Stochastic*, 1st ed. Springer International Publishing, 2015.
- [33] P. Cortes, J. Rodriguez, C. Silva, and A. Flores, "Delay compensation in model predictive current control of a three-phase inverter," *IEEE Transactions on Industrial Electronics*, vol. 59, no. 2, pp. 1323–1325, Feb. 2012.



**Yeiner Arias-E.** was born in Limón, Costa Rica. He received the B.Sc. and M.Sc. degrees in electronic engineering from the Costa Rica Institute of Technology in 2014 and 2016, respectively. He is currently working toward a Ph.D. degree at the University of Chile, Santiago, Chile. Since 2014, he has been with the Costa Rica Institute of Technology, where he is currently a Lecturer Professor. His main interests are Modular Multilevel Converters Control, Model Predictive Control and Embedded Systems.



**Roberto Cárdenas** was born in Punta Arenas, Chile. He received the B.Sc. degree in electrical engineering from the University of Magallanes, Punta Arenas, in 1988, and the M.Sc. degree in electronic engineering and the Ph.D. degree in electrical and electronic engineering from the University of Nottingham, in 1992 and 1996, respectively. He is currently a Professor of Power Electronics and Drives with the Electrical Engineering Department, University of Chile, Santiago, Chile.



**Matías Urrutia** was born in Santiago, Chile. He received the B.Sc. and M.Sc. degrees in electrical engineering from Federico Santa María Technical University (UTFSM) in 2017. Currently, Mr Urrutia is pursuing a dual-degree Ph.D. in electrical engineering offered by the University of Chile and the University of Nottingham. His main interests are Modular Multilevel Converters control and Model predictive Control.



**Matías Díaz** was born in Santiago, Chile. In 2011, he received the B.Sc. and M.Sc. degrees in electrical engineering from the University of Santiago of Chile, Santiago, Chile, and the dual Ph.D. degrees from the University of Nottingham, Nottingham, U.K., and the University of Chile, Chile, Santiago, Chile, in 2017. He is an Associate Professor with the University of Santiago, Chile. His research interests are mainly multilevel converters.



**Luca Tarisciotti** received the master's degree in electronic engineering from The University of Rome, Italy, in 2009, and the Ph.D. degree in electrical and electronic engineering from the PEMC Group, University of Nottingham, Nottingham, U.K., in 2015. He is currently working as an Assistant Professor with the University Andres Bello, Santiago, Chile. His research interests include matrix converters, dc/dc converters, multilevel converters advanced power electronics, and smart grids control.



**Jon C. Clare** was born in Bristol, U.K., in 1957. He received the B.Sc. and Ph.D. degrees in electrical engineering from the University of Bristol, U.K., in 1979 and 1990, respectively. Since 1990, he has been with the Faculty of Engineering, University of Nottingham, U.K. He is currently a Professor of Power Electronics and is the Head of the Electrical and Electronic Engineering Department. His research interests are in power-electronic converters and their applications and control.